Phase-Selective and Localized TiO₂ Coating on Additive and Wrought Titanium by Direct Laser Surface Modification Approach

Parvin Fathi-Hafshejani,¹ Haden Johnson,² Zabihollah Ahmadi,¹ Michael Roach,² Nima Shamsaei,^{3,4} Masoud Mahjouri-Samani^{1,4*}

Abstract

Titanium has been the material of interest in biological implant applications due to its unique mechanical properties and biocompatibility. Their design is now growing rapidly due to the advent of additive manufacturing technology that enables the fabrication of complex and patientcustomized parts. Titanium dioxides (TiO₂) coatings with different phases (e.g., anatase, rutile) and morphologies have shown to be effective in enhancing osteointegration and antibacterial behavior. This enhanced antibacterial behavior stems from the photocatalytic activity generated from crystalline TiO2 coatings. Anatase has commonly been shown to be a more photocatalytic oxide phase compared to rutile despite its larger bandgap. However, more recent studies have suggested a synergistic effect leading to increased photocatalytic activity may be produced with combination oxides containing both anatase and rutile phases. Here, we demonstrate the selective and localized formation of TiO2 nanostructures on additive and wrought titanium parts with anatase, rutile, and mixed phases by a laser-induced transformation approach. Compared to conventional coating processes, this technique produces desired TiO₂ phases simply by controlled laser irradiation of titanium parts in an oxygen environment, where needed. The effects of processing conditions such as laser power, scanning speed, laser pulse duration, frequency, and gas flow on the selective transformation were studied. The morphological and structural evolutions were investigated using various characterization techniques. This method is specifically of significant interest in creating selective-phase TiO₂ surfaces on titanium-based bio-implants, including those fabricated by additive manufacturing technologies.

Key Words: Bioimplant, additive manufacturing, titanium dioxide, laser processing

¹ Department of Electrical and Computer Engineering, Auburn University, Auburn, AL, USA

² The Department of Biomedical Materials Science, University of Mississippi Medical Center, Jackson, MS, USA

³ Department of Mechanical Engineering, Auburn University, Auburn, AL, USA.

⁴ National Center for Additive Manufacturing Excellence (NCAME), Auburn University, Auburn, AL, USA.

^{*}Address correspondence to mahjouri@auburn.edu

Introduction

Titanium-based parts and implants are widely used in the field of orthopedic and dental surgery because of their appropriate biocompatibility and mechanical properties such as bio-inertness, low allergenicity, excellent fatigue life, and good strength-to-weight ratio.¹⁻³ The design of such implants is growing rapidly with the advent of additive manufacturing technology that enables the fabrication of complex and patient-customized parts.⁴ Many recent efforts have been made to modify and functionalize the surface of titanium-based implants.⁵⁻¹³ Improving the antibacterial activity of titanium dioxide (TiO₂) coatings on implant materials has been reported as an attractive natural solution for improving implant surfaces, ¹⁴⁻¹⁶ for example, by depositing TiO₂ nanoparticles or nanotubes on the surface of titanium parts.¹⁷

TiO₂ nanomaterials are widely used in applications ranging from photocatalysis and energy to biomedical and sensing devices.¹⁸ Their physical properties are strongly correlated to their phases (e.g., anatase, rutile, brookite, amorphous),¹⁹ and morphologies (e.g., micro/nanostructures, porosity).²⁰⁻²² - Thus, various surface oxidation methods, such as chemical (acid and alkali) treatment, sol-gel formation, ion implantation, and thermal oxidation, have been employed to develop a functional implant surface by changing the surface properties of the native passive layer to improve osseointegration.²³⁻²⁸ Various physical, chemical, or electrochemical deposition processes are used for the synthesis of TiO₂ structures and films on titanium parts such as electrochemical anodization, chemical vapor deposition, pulse laser deposition, thermal and plasma spray, and sputtering techniques.^{19, 29-37}

Anodization is a technique that expands the thickness of the natural oxide layer on the surface of metal components.³⁸ These methods have been successful in providing uniform coatings of specific TiO₂ phases.³⁹⁻⁴¹ Anodized anatase surfaces have commonly shown higher photocatalytic activity than rutile surfaces leading to an enhanced antimicrobial effect.⁴²⁻⁴⁴ More recent studies have shown mixed-phase oxides, containing both anatase and rutile, to exhibit a synergistic effect with increased photocatalytic activity.⁴⁵⁻⁴⁶ In mixed-phase oxides, differences in the band gaps extend the lifetime of the electron-hole pairs and thus increase the generation of free radicals.⁴⁷ For this synergistic effect to occur, the anatase and rutile phases need to be in close spatial proximity to each other. Anodization methods are not able to provide localized, selective phase and patterned coatings, especially on parts with complex geometries. Therefore, the development of a facile method that allows the formation of phase-specific, location-specific, and patternable TiO₂ nanostructures on the complex titanium parts is highly desirable for the medical sector.

Additionally, the complexity of the implants' shape and multi-interfaces with various tissues in the body requires the ability to selectively and locally deposit specific phases and morphologies of TiO₂ on various locations of implants, making it extremely challenging using conventional coating methods. This is specifically true for additively manufactured implants that can be customized per patient and injury. The freedom in design offered by additive manufacturing technologies is revolutionizing the implant industry by introducing customized implants that often have more complex geometries. Due to such complexities, not only are more location-specific depositions needed, but it also requires an accurate method to precisely deposit on confined regions of the implant.

Here, we report a novel laser processing method for localized, phase-selective, and pattered TiO₂ nanostructures directly on the titanium samples as desired. In this method, a tunable nanosecond fiber laser (1064 nm wavelength) with pulse-widths ranging from 5–2000 ns, pulse energy ranging from 0.04 to 1.57 mJ, and repetition rate ranging from 1 Hz to 4160 kHz was used for the controlled surface modifications. The laser beam was coupled into a galvo scanner with an F-theta lens providing 18 µm focal size and scan speed ranging from 1 to 5000 mm/s. This allowed us to locally process the titanium parts in a controlled oxygen environment to accurately induce structural, chemical, and phase transformations. After reactions, a thin film of TiO₂ nanoparticles formed on the titanium parts. By tuning the processing parameters, different TiO₂ phases (e.g., rutile, anatase, mixed) and patterns were generated on the surfaces of titanium samples where desired.

Results and Discussion

Lasers provide the ability to accurately deliver a precise amount of energy onto a confined region of a material in order to achieve the desired response. For opaque materials, this energy is absorbed near the surface, modifying the surface chemistry, crystal structure, and/or multiscale morphology without altering the bulk material. The non-equilibrium processes in the high energy laser-material interaction dynamics can overcome energy barriers required for chemical reactions and increase their reaction kinetics far beyond equilibrium processes.⁴⁸⁻⁵⁰ In this method, irradiation of the material with short laser leads to rapid heating of the surface of the material as well as the formation of high-temperature plasma that prepares the bed for oxygen dissociation and its reaction with titanium. With this dry and clean technique, high-purity TiO₂ coatings with controlled phases and morphologies can be synthesized on the surface of titanium samples. **Figure 1** shows the schematic illustration of the fabrication process. By scanning the titanium surface with this tunable laser, titanium, and oxygen controllably react to form the porous structures of TiO₂ with specific phases on the surface of the titanium sample. A comprehensive experimental study was performed to understand and control this process.

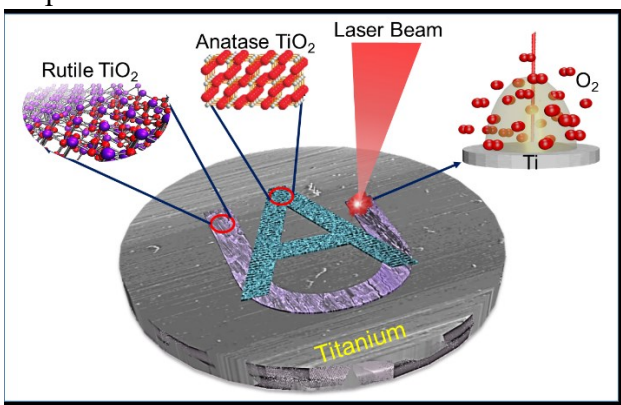


Figure 1. Schematic illustration showing the patterned, localized, and phase-selective fabrication of anatase and rutile TiO₂ nanostructures on the titanium samples by a controlled laser surface modification approach.

We first focused on understanding how the laser parameters, and hence, the surface coupled energy can govern the evolution of phase and morphology of the formed TiO₂ micro/nanostructures. The amount of coupled energy in this process is mainly the combination pulse-width, focus point, repetition rate, and scan speed of the laser. Therefore, we performed a systematic study under

various process parameters including laser power ranging from 13W to 71W with six scan speeds (100, 200, 500, 1000, 2000, 5000 mm/s), and six factory-set pulse-widths (10, 108, 261, 508, 1020, 2020 ns). Through these studies, we demonstrated the crystallization dynamics, identified the energy thresholds, and found all possible transformation and non-interacting zones. Four types of titanium samples, including additive manufactured as well as commercial wrought TAV (Ti-6Al-4V grade 5), CP Titanium Grade 4, and pure titanium (99.99 purity), were tested in this study.

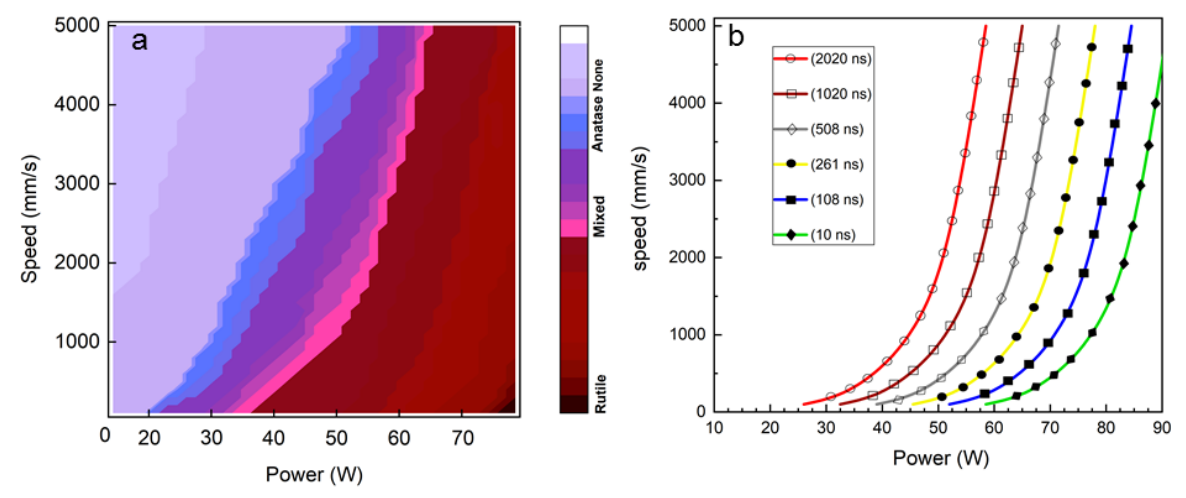


Figure 2. Comprehensive map (a) of the pure titanium (purity 99.99%) response to different laser powers and scan speed under atmospheric oxygen pressure and 0.1 SLM oxygen flow. Blue, red, and purple zones show the process regions where anatase, rutile, and mixed phases form during the process, respectively. The effect of pulse-width on the transformation process (b). The lines in Figure 2b indicate the anatase to rutile transition boundary where mixed rutile and anatase phases coexist. Pure anatase and rutile phases exist to the left and right of the lines for each waveform, respectively.

Figure 2 shows the effect of laser power, scan speed, and pulse-width on the formation of anatase, rutile, and mixed-phase on the titanium samples. **Figure 2a** shows a heatmap of the unaffected, anatase, mixed anatase/rutile, and rutile formation zones as a function of laser power and scan speed using the laser pulse-width of 508 nm and PRF0 frequency of 108 kHz on pure titanium sheets (purity 99.99%). The line hatch has 40% overlap, while the pulse overlap (pitch) varies by the scan speed. In this case, the energy per pulse ranges from 0.125 mJ for 13.5 W power to 0.687 mJ for 74W power with the fluence of 47 J/cm² and 270 J/cm², respectively. It should be noted that the energy per pulse is constant for all the frequencies used in this work since the chosen frequencies are below the PRF0 value for each waveform, according to the laser operating manual. PRF0 is the minimum frequency that gives maximum average power (defined by the active current setpoint). For PRF > PRF0, pulse energies and peak powers decrease so that the average power does not exceed the rated power of the laser module.

In general, higher laser powers and/or slower scan speeds tend to induce rutile formation by inducing more heat, while lower laser power and/or faster scan speed change the kinetics toward the anatase formation zone by inducing less heat. It was observed that the rutile zone (red), where the best quality rutile crystals form, was much wider than the anatase and mixed-phase zones. Above this red zone, due to extreme temperatures, samples ignite and burn. As it is apparent from the narrow crystallization window of the anatase (blue), its formation required a very deliberate process parameter control that otherwise could easily transform into mixed or rutile phases. The

process parameter zone in between anatase and rutile generated mixed anatase/rutile phases (purple). Furthermore, the pulse-width study (Figure 2b) showed that increasing the pulse duration would result in a left shift in the power and speed relationship plots. This infers that the longer pulse durations induce more heat than that of shorter pulses, which in turn requires less power or more speed in order to balance for the required transformation energies in each zone.

We further studied the effect of distance between the processing lines (hatch) and overlap between the pulses (overlapping). We found that these processing parameters have a significant impact on the phase and morphology evolution of the final TiO₂ structures. In addition, the role of the laser repetition rate (frequency) that dictates the time between the consecutive pulses found to be important in the transformation process. For instance, at lower frequencies (e.g., 20 kHz), the off-time between the pulses increases, providing more cooling time before the next pulse arrives. This fast heat quenching of the reaction in each pulse resulted in the formation of anatase nanoparticles that stick well to the surface. We, therefore, designed a systematic experiment to track the impact of overlapping pulses and the off-time between the consecutive pulses employing the best speed and power parameters found in the previous experiment, which could produce better anatase, rutile, and mixed phases.

As expected, at lower frequencies (e.g., 20 kHz), the off-time between pulses is 49.5 µs which provides the material enough time to cool between the pulses resulting in the formation of highquality anatase structures. At higher frequencies (e.g., 100 kHz), the off-time between pulses becomes 9.5 µs resulting in heat accumulation, and hence, the formation of high-quality rutile TiO₂ structures. It should be noted that the energy per pulse does not change by changing the repetition rate as long as it is below the maximum allowable frequency defined by the manufacturer (SPI Lasers). Similarly, using less overlap (e.g., 0%) between the processed spots formed anatase structures while more overlap (e.g., 90%) formed rutile structures due to the overheating/reheating. In addition, reprocessing of formed anatase phase transformed it into the rutile phase. Table 1 shows an example of the optimized process parameters by which the high-quality anatase, rutile, and mixed-phase TiO₂ coatings were produced, according to Raman and X-ray diffraction (XRD) measurements described below. Although Table 1 was optimized for wrought TAV samples, the same set of parameters also tested on wrought CP Ti, additive, and pure titanium (see Supporting Information) that created similar expected results. The results on the wrought CPTi samples were comparable had the same quality results as wrought TAV. The results on the additive and pure titanium samples could be further improved by fine-tuning these parameters.

 Table 1. Laser parameters to synthesize different titanium phases

TiO ₂	Laser	Scan	Pulse-	Pulse	Pulse	Gas Flow	Pulse	Line	Frequency
Phase	Power	Speed	width	energy	fluence	rate	overlap	Hatch	(kHz)
	(W)	(mm/s)	(ns)	(mJ)	(J/cm ²)	(SLM)	(%)	(%)	
Anatase	12.5	400	508	0.625	246	25.6	0	40	20
Mixed	67.5	400	508	0.337	133	25.6	50	0	200
Rutile	62.5	200	508	0.625	246	21.3	90	0	100

To monitor the transformation process and identify the formed TiO₂ phases on the titanium samples, we performed Raman and glancing angle XRD spectroscopy. Also, to evaluate the quality of our laser-generated TiO₂ samples, their Raman signatures were compared with that of

commercially available anatase and rutile powders, both showing similar signatures (see Supporting Information). The Raman spectra were acquired using a 532 nm laser excitation source, a 10x objective lens, and 1200 lmm⁻¹ grating. **Figure 3a** shows the Raman spectra obtained from the anatase, rutile, and mixed-phase in this experiment. Anatase samples showed clear Raman peaks at 145, 198, 399, 516, and 638 cm⁻¹, while rutile samples showed peaks 241, 445, 610 cm⁻¹. The samples with mixed phases have the signature of both anatase and rutile. These Raman results were similar to the results reported in the literature⁵¹, confirming the successful formation of various TiO₂ phases in this process. The transformation quality was similar for all samples used in this experiment, including additively manufactured and wrought TAV, wrought CP Ti Grade 4, and pure titanium samples.

Figure 3b shows the XRD results from wrought TAV samples. Peaks at 25.3°, which verify the presence of anatase phase, are present on the anatase and mixed-phase specimens. The peak at 27.5° on rutile and mixed-phase specimens confirm the formation of rutile. The weight fractions of anatase and rutile in the oxide layer of representative specimens from each group were calculated using the following Spurr and Myers equation: ⁵²

$$X_A = \frac{1}{1 + 1.26 \left(\frac{I_R}{I_A}\right)}$$
$$X_R = 1 - X_A$$

where X_R and X_A are the weight percentages of rutile and anatase, and I_R and I_A are the intensities of the diffraction peaks for rutile (110) and anatase (101), respectively. The phase ratio for the mixed-phase oxide shown in Figure 3b was 37% anatase and 63% rutile. Similar results were also obtained for the additively manufactured and pure titanium samples (see Supporting Information). These results verify and support the findings observed using Raman spectroscopy.

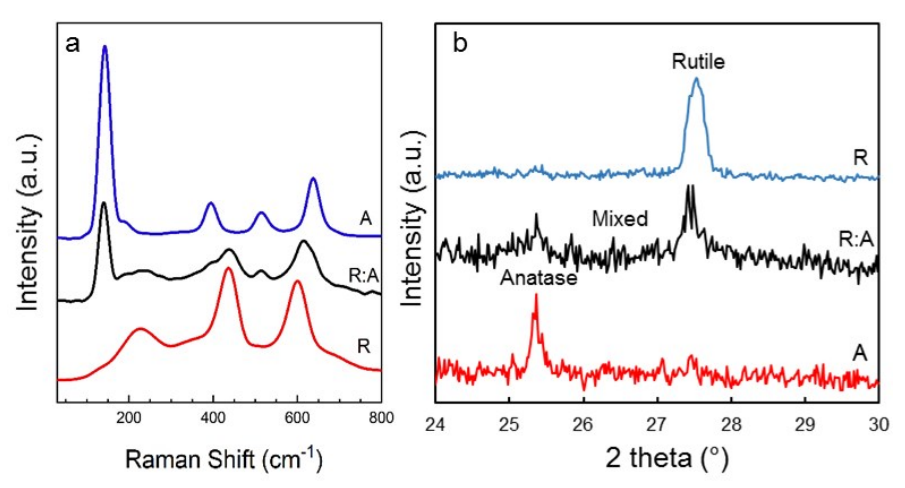


Figure 3. Representative Raman spectra (a) and XRD scans (b) of the synthesized TiO₂ structures on wrought TAV samples showing the successful formation of anatase, mixed-phase, and rutile peaks.

To analyze the surface morphology and physical structure of the synthesized TiO₂ samples in this process, we performed optical microscopy, laser confocal microscopy, and scanning electron

microscopy (SEM) to obtain information at various length scales. **Figure 4a-f** show the laser confocal 2D images (a, c, e) and corresponding 3D surface profiles (b, d, f) of the synthesized anatase, mixed-phase, and rutile samples, respectively. Representative surface roughness (Ra) values for anatase, mixed-phase, and rutile wrought TAV samples were 5.17 μ m, 4.69 μ m, and 4.72 μ m, respectively. Optical microscopy images for additively manufactured TAV and pure titanium (purity 99.99%) samples have been shown in figures S2 and S5 of the Supporting Information.

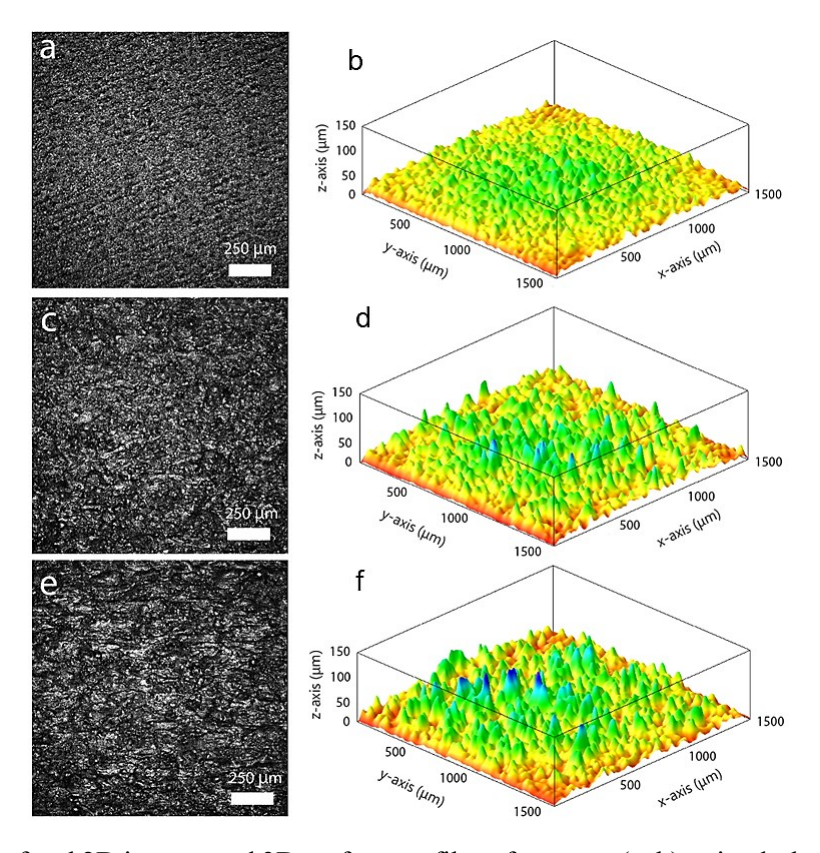


Figure 4. Laser confocal 2D images and 3D surface profiles of anatase, (a, b), mixed-phase (c, d), and rutile (e, f) TiO₂ wrought TAV samples.

Figure 5 shows the SEM images of the anatase, mixed-phase, and rutile TiO_2 formed on the surface of wrought TAV samples. The size and morphology of the anatase samples were micro/nanostructures with porous morphology, as shown in **Figure 5a,b**. As seen in **Figure 5e,f**, the rutile TiO_2 on wrought TAV were larger crystals with big cracks showing the ceramic nature of the rutile structures. Additionally, both cracks and porous structures were produced on the mixed-phase surface, as shown in **Figure 5c,d**. SEM images for titanium sheets (purity 99.99%) and additive manufactured samples show a similar trend (see Supporting Information). Based on the cross-section SEM images of the laser modified wrought TAV, the anatase layer looked mesoporous with a thickness of ~0.2–0.5 μm, whereas the thickness of mixed-phase and rutile became gradually thicker with ~0.4 μm and ~2 μm, respectively (see Supporting Information).

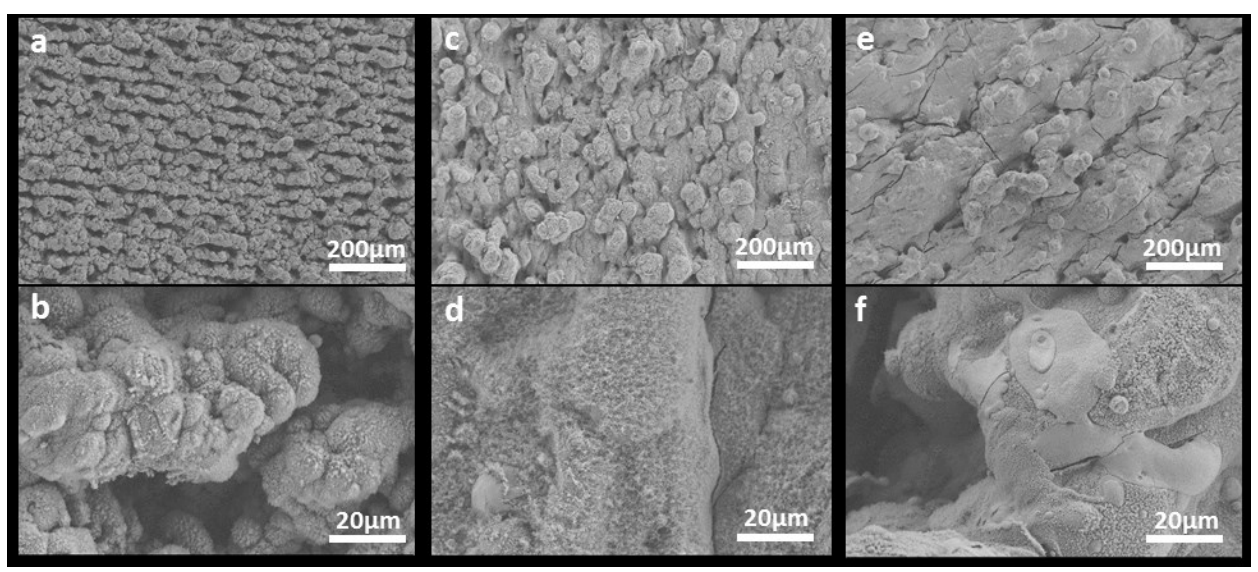


Figure 5. SEM images showing the morphology of the wrought TAV TiO₂ anatase (a, b), mixed-phase (c, d), and rutile (e, f) nanostructures. Smaller features with micro/nanostructures and mesoporous morphology were observed for anatase samples. The feature became larger and denser for rutile samples.

One of the most noticeable advantages of this method, specifically for the customized additive manufactured implants, is its ability for the selective and localized synthesis of various phases, shapes, sizes, and patterns side-by-side without the need for any conventional patterning or lithography and deposition processes. This unique laser processing method allows us to design desired TiO₂ structures on beneficial locations on the bioimplant surfaces. We have successfully synthesized rutile, anatase, and mixed-phase TiO₂ structures with designed patterns and matrices. **Figure 6a-c** shows the optical images of various rutile/anatase patterns side-by-side in checkerboard, concentric circles, and AU logo designs. **Figure 6d, e** shows the corresponding Raman spectra obtained from anatase and rutile as labeled.

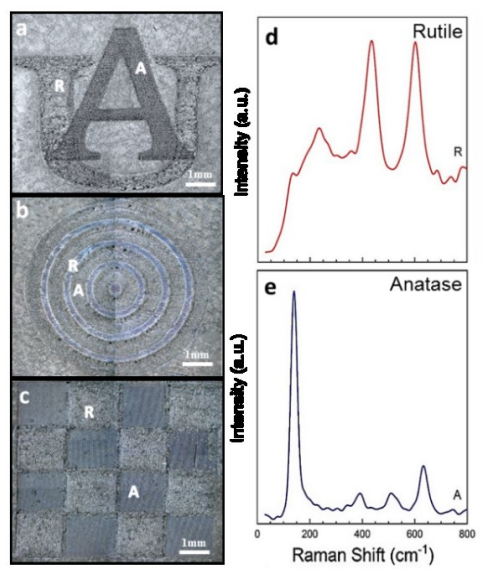


Figure 6. Selective and localized formation of anatase and rutile TiO₂, side-by-side. Optical images show Auburn University logo (a), concentric circular patterns (b), and checkers board (c) consisting of anatase and rutile TiO₂, side-by-side. Representative Raman spectra obtained from the rutile (d) and anatase (e) regions as labeled.

Conclusion

In conclusion, we demonstrated the localized, selective, and patterned synthesis of various TiO₂ phases and structures by controlled laser transformation of titanium surface. Anatase, mixed-phase, and rutile TiO₂ were formed by precisely tuning the laser interaction with titanium in an oxygen environment. The laser interaction with titanium was controlled by laser power, scan speed, and pulse-width. We showed that longer pulse-width, slower scan speeds, and higher laser powers led to the formation of rutile phases, while shorter pulse-width, lower laser power, and faster scan speed resulted in the formation of anatase TiO₂. Processing parameters in between formed mixed rutile/anatase TiO₂. We also showed the effect of overlapping of pulses on phase transformation. More overlaps resulted in phase transformation toward rutile TiO₂ and vice versa. The method offers a simple, clean, and fast formation of TiO₂ coating on titanium bioimplants, specifically the customized, additively manufactured ones, with the preferred phases, structures, and patterns where desired.

Materials and Method

Sample preparation. We used four different types of titanium products, including pure titanium (purity 99.99%) sheets (10×10 mm squares, 1000 test surfaces), additively manufactured (10 mm in diameter, 60 test surfaces), wrought TAV (15 mm in diameter, 30 test surfaces), and CP Ti Grade 4 (15 mm in diameter, 30 test surfaces) samples in these experiments. CP Ti Grade 4, TAV, and pure titanium were obtained from commercial vendors. Additively manufactured samples were prepared using EOS M290 machine, a laser beam powder bed fusion (LB-PBF) additive manufacturing process, with the manufacturer's recommended process parameters of 280 W laser power, 0.14 mm hatching space, 1200 mm/s scanning speed and 30 μ m layer thickness using Ti-6Al-4V Powder: LPW-Ti64GD23-AAFD.

 TiO_2 formation process. First, the titanium samples were cleaned by acetone and methanol and placed into a custom-built environmental chamber for laser processing. The laser transformation experiments were performed in an oxygen environment with different flow rates (6-60 slm) and at room temperature. The chamber was first flushed with oxygen gas for two minutes to ensure the removal of possible air contaminants. Samples were then controllably laser processed by a 130 W tunable nanosecond fiber laser (1064 nm wavelength), S-type beam with beam quality(M^2) 1.3, beam diameter prior to focusing 9.5 mm with pulse-width ranging from 5–2000 ns, pulse energy ranging from 0.04 to 1.57 mJ, and repetition rate ranging from 1 Hz to 4160 kHz. The laser beam was coupled into a galvo scanner with an F-theta lens with 103 mm focal length producing 18 μ m focal size and scan speed ranging from 1 to 5000 mm/s. A laser marking software (Laser Studio Professional) was used to design various patterns and control the process parameters (e.g., power, pulse-width, number of pulses, scan speed, repetition rate, and overlap) for each specific pattern.

Raman Spectroscopy. A custom-made Raman spectroscopy system was used for optical diagnostics of our laser synthesized TiO_2 samples. The measurements were performed in a confocal micro configuration using a 10x microscope objective lens (NA = 0.25). We used a Horiba HR spectrometer with 1200 grooves/mm grating and a laser excitation wavelength of 532 nm for Raman acquisition.

XRD measurements: Thin-film X-ray diffraction (XRD) (Scintag XDS 2000, Franklin, MA) was used to further verify the formation of crystalline TiO_2 in these experiments. Samples were rotated 1° away from the copper X-ray source (1.54 Å Cu-K α) to enhance the X-ray interaction volume with the surface layer. Scans were conducted between two-theta angles ranging from 24° to 30° at a continuous scan rate of 2° /min. Anatase and rutile have their highest intensity diffraction peaks within this range at 25.3° and 27.5° , respectively. Jade software (Jade 9 MDI, Livermore, CA) was used to identify diffraction peaks.

Morphology and structure analysis. A scanning electron microscope (SEM: Zeiss Supra 40, Jena, Germany,) with an accelerating voltage of 3 kV was used to examine the surface morphology of the laser synthesized oxides at different magnifications. Laser confocal microscopy (Leica TCS SP2, Wetzler, Germany) was used to measure surface roughness of the oxides. The total scan area for each specimen was 1500 μm X 1500 μm, and a 1 μm z-axis step size was used. Fiji software was used to process raw image data and build 3-D surface profiles of the oxide surfaces. ⁵³

Acknowledgments

This material is based upon work partially supported by the U.S. National Science Foundation (NSF) under grant No. 1923363, and Auburn University Intermural Grant Program (IGP-VPR 180247). The authors would like to thank Fort Wayne Metals (Fort Wayne, IN) for the donations of the wrought TAV and CP Ti Grade 4 materials for the study.

Supporting Information Available

Supporting Information is available online. The Supporting information includes results for: additively manufactured TAV samples, high purity wrought Ti samples, wrought CP Ti grade 4 samples, cross-section SEM images of wrought TAV, TiO₂ quality comparison of laser-generated TiO₂ versus commercial powers, and roughness values before laser processing.

Author Contributions

P.F. designed and performed laser synthesis and processing experiments, materials characterization, and data analysis. Z.A. participated in the laser processing experiment. M.R. and H. J. participated in XRD and SEM characterization, data analysis, and manuscript preparation. N.S. participated in the experimental design, additive manufacturing sample preparation, and discussions on experimental results. M.M.S. led the project, participated in experimental design, data acquisition and analysis, discussions, and manuscript preparation. All of the authors commented on the manuscript.

Conflict of Interest

The authors declare no conflict of interest.

Reference

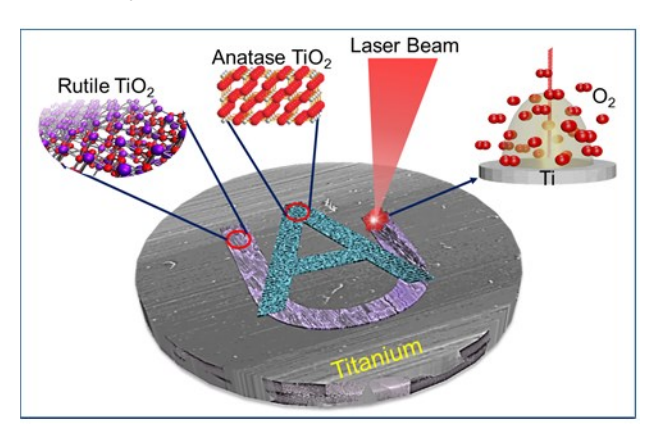
- 1. Adell, R.; Eriksson, B.; Lekholm, U.; Brånemark, P.-I.; Jemt, T., A long-term follow-up study of osseointegrated implants in the treatment of totally edentulous jaws. *International Journal of Oral & Maxillofacial Implants* **1990**, *5* (4).
- 2. Geetha, M.; Singh, A.; Asokamani, R.; Gogia, A., Ti based biomaterials, the ultimate choice for orthopaedic implants—a review. *Progress in materials science* **2009**, *54* (3), 397-425.
- 3. Carrion, P. E.; Shamsaei, N.; Daniewicz, S. R.; Moser, R. D., Fatigue behavior of Ti-6Al-4V ELI including mean stress effects. *International Journal of Fatigue* **2017**, *99*, 87-100.
- 4. Sidambe, A., Biocompatibility of advanced manufactured titanium implants—A review. *Materials* **2014**, *7* (12), 8168-8188.
- 5. Liu, X.; Chu, P. K.; Ding, C., Surface modification of titanium, titanium alloys, and related materials for biomedical applications. *Materials Science and Engineering: R: Reports* **2004**, *47* (3-4), 49-121.
- 6. Kulangara, K.; Leong, K. W., Substrate topography shapes cell function. *Soft Matter* **2009**, *5* (21), 4072-4076.
- 7. Williams, D. F., On the nature of biomaterials. *Biomaterials* **2009**, *30* (30), 5897-5909.
- 8. Higuchi, A.; Ling, Q.-D.; Chang, Y.; Hsu, S.-T.; Umezawa, A., Physical cues of biomaterials guide stem cell differentiation fate. *Chemical reviews* **2013**, *113* (5), 3297-3328.
- 9. Fattakhova-Rohlfing, D.; Zaleska, A.; Bein, T., Three-dimensional titanium dioxide nanomaterials. *Chemical reviews* **2014**, *114* (19), 9487-9558.
- 10. Cho, I. S.; Chen, Z.; Forman, A. J.; Kim, D. R.; Rao, P. M.; Jaramillo, T. F.; Zheng, X., Branched TiO2 nanorods for photoelectrochemical hydrogen production. *Nano Letters* **2011**, *11* (11), 4978-4984.
- 11. Crane, G. M.; Ishaug, S. L.; Mikos, A. G., Bone tissue engineering. Nature Publishing Group: 1995.
- 12. Jokinen, M.; Pätsi, M.; Rahiala, H.; Peltola, T.; Ritala, M.; Rosenholm, J., Influence of sol and surface properties on in vitro bioactivity of sol-gel-derived TiO2 and TiO2-SiO2 films deposited by dip-coating method. *Journal of Biomedical Materials Research: An Official Journal of The Society for Biomaterials, The Japanese Society for Biomaterials, and the Australian Society for Biomaterials* **1998**, 42 (2), 295-302.
- 13. Nygren, H.; Eriksson, C.; Lausmaa, J., Adhesion and activation of platelets and polymorphonuclear granulocyte cells at TiO2 surfaces. *Journal of Laboratory and Clinical Medicine* **1997**, *129* (1), 35-46.
- 14. Nakata, K.; Fujishima, A., TiO2 photocatalysis: Design and applications. *Journal of photochemistry and photobiology C: Photochemistry Reviews* **2012**, *13* (3), 169-189.
- 15. Bao, S.-J.; Lei, C.; Xu, M.-W.; Cai, C.-J.; Jia, D.-Z., Environment-friendly biomimetic synthesis of TiO2 nanomaterials for photocatalytic application. *Nanotechnology* **2012**, *23* (20), 205601.
- 16. Biswas, S.; Becker, U., Molecular modeling of cell adhesion peptides on hydroxyapatite and TiO2 surfaces: implication in biomedical implant devices. *Journal of Biomaterials and Nanobiotechnology* **2013**, *4* (04), 351.
- 17. Ahn, T.-K.; Lee, D. H.; Kim, T.-s.; chol Jang, G.; Choi, S.; Oh, J. B.; Ye, G.; Lee, S., Modification of titanium implant and titanium dioxide for bone tissue engineering. In *Novel Biomaterials for Regenerative Medicine*, Springer: 2018; pp 355-368.

- 18. Wu, S.; Weng, Z.; Liu, X.; Yeung, K.; Chu, P. K., Functionalized TiO2 based nanomaterials for biomedical applications. *Advanced functional materials* **2014**, *24* (35), 5464-5481.
- 19. Löbl, P.; Huppertz, M.; Mergel, D., Nucleation and growth in TiO2 films prepared by sputtering and evaporation. *Thin solid films* **1994**, *251* (1), 72-79.
- 20. Zhao, T.; Zhao, Y.; Jiang, L., Nano-/microstructure improved photocatalytic activities of semiconductors. *Philosophical Transactions of the Royal Society A: Mathematical, Physical and Engineering Sciences* **2013**, *371* (2000), 20120303 %@ 1364-503X.
- 21. Asahi, R.; Morikawa, T.; Irie, H.; Ohwaki, T., Nitrogen-doped titanium dioxide as visible-light-sensitive photocatalyst: designs, developments, and prospects. *Chemical reviews* **2014**, *114* (19), 9824-9852 %@ 0009-2665.
- 22. Pearson, A.; Zheng, H.; Kalantar-Zadeh, K.; Bhargava, S. K.; Bansal, V., Decoration of TiO2 nanotubes with metal nanoparticles using polyoxometalate as a UV-switchable reducing agent for enhanced visible and solar light photocatalysis. *Langmuir* **2012**, *28* (40), 14470-14475.
- 23. Park, E.-J.; Song, Y.-H.; Hwang, M.-J.; Song, H.-J.; Park, Y.-J., Surface characterization and osteoconductivity evaluation of micro/nano surface formed on titanium using anodic oxidation combined with H2O2 etching and hydrothermal treatment. *Journal of nanoscience and nanotechnology* **2015**, *15* (8), 6133-6136.
- 24. Kokubo, T.; Yamaguchi, S., Suppl 1-M2: Bioactive Titanate Layers Formed on Titanium and Its Alloys by Simple Chemical and Heat Treatments. *The open biomedical engineering journal* **2015**, *9*, 29.
- 25. Roest, R.; Latella, B.; Heness, G.; Ben-Nissan, B., Adhesion of sol-gel derived hydroxyapatite nanocoatings on anodised pure titanium and titanium (Ti6Al4V) alloy substrates. *Surface and Coatings Technology* **2011**, *205* (11), 3520-3529.
- 26. Huang, H.; Lan, P.-H.; Zhang, Y.-Q.; Li, X.-K.; Zhang, X.; Yuan, C.-F.; Zheng, X.-B.; Guo, Z., Surface characterization and in vivo performance of plasma-sprayed hydroxyapatite-coated porous Ti6Al4V implants generated by electron beam melting. *Surface and Coatings Technology* **2015**, *283*, 80-88.
- 27. Jin, G.; Qin, H.; Cao, H.; Qian, S.; Zhao, Y.; Peng, X.; Zhang, X.; Liu, X.; Chu, P. K., Synergistic effects of dual Zn/Ag ion implantation in osteogenic activity and antibacterial ability of titanium. *Biomaterials* **2014**, *35* (27), 7699-7713.
- 28. Tan, A.; Ismail, R.; Chua, K.; Ahmad, R.; Akbar, S.; Pingguan-Murphy, B., Osteogenic potential of in situ TiO2 nanowire surfaces formed by thermal oxidation of titanium alloy substrate. *Applied surface science* **2014**, *320*, 161-170.
- 29. Mahjouri-Samani, M.; Tian, M.; Puretzky, A. A.; Chi, M.; Wang, K.; Duscher, G.; Rouleau, C. M.; Eres, G.; Yoon, M.; Lasseter, J., Nonequilibrium synthesis of TiO2 nanoparticle "building blocks" for crystal growth by sequential attachment in pulsed laser deposition. *Nano letters* **2017**, *17* (8), 4624-4633.
- 30. Tian, M.; Mahjouri-Samani, M.; Eres, G.; Sachan, R.; Yoon, M.; Chisholm, M. F.; Wang, K.; Puretzky, A. A.; Rouleau, C. M.; Geohegan, D. B., Structure and formation mechanism of black TiO2 nanoparticles. *ACS nano* **2015**, *9* (10), 10482-10488.
- 31. Dumitriu, D.; Bally, A.; Ballif, C.; Hones, P.; Schmid, P.; Sanjines, R.; Levy, F.; Parvulescu, V., Photocatalytic degradation of phenol by TiO2 thin films prepared by sputtering. *Applied Catalysis B: Environmental* **2000**, *25* (2-3), 83-92.
- 32. Takeda, S.; Suzuki, S.; Odaka, H.; Hosono, H., Photocatalytic TiO2 thin film deposited onto glass by DC magnetron sputtering. *Thin solid films* **2001**, *392* (2), 338-344.

- 33. Zhang, F.; Huang, N.; Yang, P.; Zeng, X.; Mao, Y.; Zheng, Z.; Zhou, Z.; Liu, X., Blood compatibility of titanium oxide prepared by ion-beam-enhanced deposition. *Surface and Coatings Technology* **1996**, *84* (1-3), 476-479.
- 34. Gaviria, L.; Salcido, J. P.; Guda, T.; Ong, J. L., Current trends in dental implants. *Journal of the Korean Association of Oral and Maxillofacial Surgeons* **2014**, *40* (2), 50-60.
- 35. Lifland, M.; Kim, D.; Okazaki, K., Mechanical properties of a Ti-6A1–4V dental implant produced by electro-discharge compaction. *Clinical materials* **1993**, *14* (1), 13-19.
- 36. Wang, X.; Li, Y.; Hodgson, P. D.; Wen, C. e., Biomimetic modification of porous TiNbZr alloy scaffold for bone tissue engineering. *Tissue Engineering Part A* **2009**, *16* (1), 309-316.
- 37. Yang, B.; Mahjouri-Samani, M.; Rouleau, C. M.; Geohegan, D. B.; Xiao, K., Low temperature synthesis of hierarchical TiO 2 nanostructures for high performance perovskite solar cells by pulsed laser deposition. *Physical Chemistry Chemical Physics* **2016**, *18* (39), 27067-27072.
- 38. Benea, L.; Mardare-Danaila, E.; Celis, J.-P., Increasing the tribological performances of Ti–6Al–4V alloy by forming a thin nanoporous TiO2 layer and hydroxyapatite electrodeposition under lubricated conditions. *Tribology International* **2014**, *78*, 168-175.
- 39. Cheng, Y.; Yang, H.; Yang, Y.; Huang, J.; Wu, K.; Chen, Z.; Wang, X.; Lin, C.; Lai, Y., Progress in TiO 2 nanotube coatings for biomedical applications: a review. *Journal of Materials Chemistry B* **2018**, *6* (13), 1862-1886.
- 40. Jain, S.; Scott Williamson, R.; Roach, M. D., Surface characterization, shear strength, and bioactivity of anodized titanium prepared in mixed-acid electrolytes. *Surface and Coatings Technology* **2017**, *325*, 594-603.
- 41. Roach, M. D.; Williamson, R. S.; Blakely, I. P.; Didier, L. M., Tuning anatase and rutile phase ratios and nanoscale surface features by anodization processing onto titanium substrate surfaces. *Materials Science and Engineering:* C 2016, 58, 213-223.
- 42. Joo, H.-C.; Lim, Y.-J.; Kim, M.-J.; Kwon, H.-B.; Han, J.-H., Characterization on titanium surfaces and its effect on photocatalytic bactericidal activity. *Applied Surface Science* **2010**, *257* (3), 741-746.
- 43. Sumita, T.; Yamaki, T.; Yamamoto, S.; Miyashita, A., Photo-induced surface charge separation of highly oriented TiO2 anatase and rutile thin films. *Applied Surface Science* **2002**, 200 (1-4), 21-26.
- 44. Luttrell, T.; Halpegamage, S.; Tao, J.; Kramer, A.; Sutter, E.; Batzill, M., Why is anatase a better photocatalyst than rutile? Model studies on epitaxial TiO2 films. *Scientific Reports* **2014**, *4* (1).
- 45. Bickley, R. I.; Gonzalez-Carreno, T.; Lees, J. S.; Palmisano, L.; Tilley, R. J. D., A structural investigation of titanium dioxide photocatalysts. *Journal of Solid State Chemistry* **1991**, *92* (1), 178-190.
- 46. Su, R.; Bechstein, R.; Sø, L.; Vang, R. T.; Sillassen, M.; Esbjörnsson, B.; Palmqvist, A.; Besenbacher, F., How the Anatase-to-Rutile Ratio Influences the Photoreactivity of TiO2. *The Journal of Physical Chemistry C* **2011**, *115* (49), 24287-24292.
- 47. Hurum, D. C.; Agrios, A. G.; Gray, K. A.; Rajh, T.; Thurnauer, M. C., Explaining the Enhanced Photocatalytic Activity of Degussa P25 Mixed-Phase TiO2Using EPR. *The Journal of Physical Chemistry B* **2003**, *107* (19), 4545-4549.
- 48. Xiong, W.; Zhou, Y.; Hou, W.; Jiang, L.; Mahjouri-Samani, M.; Park, J.; He, X.; Gao, Y.; Fan, L.; Baldacchini, T., Laser-based micro/nanofabrication in one, two and three dimensions. *Frontiers of Optoelectronics* **2015**, *8* (4), 351-378.

- 49. Wang, X.; Xu, X., Thermoelastic wave induced by pulsed laser heating. *Applied Physics A* **2001,** *73* (1), 107-114.
- 50. Xiong, W.; Zhou, Y.; He, X.; Gao, Y.; Mahjouri-Samani, M.; Baldacchini, T.; Lu, Y. In *Three-dimensional micro/nano-fabrication by integration of additive and subtractive femtosecond-laser direct writing processes*, International Congress on Applications of Lasers & Electro-Optics, LIA: 2012; pp 1160-1164.
- 51. Su, W.; Zhang, J.; Feng, Z.; Chen, T.; Ying, P.; Li, C., Surface phases of TiO2 nanoparticles studied by UV Raman spectroscopy and FT-IR spectroscopy. *The Journal of Physical Chemistry C* **2008**, *112* (20), 7710-7716.
- 52. Spurr, R. A.; Myers, H., Quantitative Analysis of Anatase-Rutile Mixtures with an X-Ray Diffractometer. *Analytical Chemistry* **1957**, *29* (5), 760-762.
- 53. Schindelin, J.; Arganda-Carreras, I.; Frise, E.; Kaynig, V.; Longair, M.; Pietzsch, T.; Preibisch, S.; Rueden, C.; Saalfeld, S.; Schmid, B.; Tinevez, J.-Y.; White, D. J.; Hartenstein, V.; Eliceiri, K.; Tomancak, P.; Cardona, A., Fiji: an open-source platform for biological-image analysis. *Nature Methods* **2012**, *9* (7), 676-682.

For Table of Contents Only



Supporting Information (SI)

Phase-Selective and Localized TiO₂ Coating on Additive and Wrought Titanium by Direct Laser Surface Modification Approach

Parvin Fathi-Hafshejani,¹ Haden Johnson,² Zabihollah Ahmadi,¹ Michael Roach,² Nima Shamsaei,^{3,4} Masoud Mahjouri-Samani^{1,4*}

In this study, four different types of titanium products were used, including wrought pure titanium (purity 99.99%), additively manufactured TAV (10 mm in diameter), wrought TAV(15 mm in diameter), and wrought CP Ti (15 mm in diameter) samples. The morphological and structural evolutions of these samples were investigated using various characterization techniques including scanning electron microscopy (SEM), X-ray diffraction (XRD), and Raman spectroscopy similar to the one in the main manuscript. To avoid redundancy in the main manuscript, one set is included in the main manuscript, and the rest are in this supplementary information.

Additively Manufactured TAV Samples:

Composition and process parameters: Ti-6Al-4V Powder: LPW-Ti64GD23-AAFD

Chemicals	Al	С	Fe	Н	N	О	Ti	V	Others	All others
Wt (%)	6.5	0.02	0.2	0.002	0.01	0.11	Bal	3.9	< 0.1	<0.4

Process parameters:

Laser Power	280 W
Scan Speed	1200 mm/s
Hatch distance	0.140 mm
Stripe width	100 mm
Layer thickness	30 mm

For these additive samples, we performed laser processing on both as-printed and polished surfaces. It should be noted that we did not observe a significant difference in the overall outcome. This could be due to the fact that the focal depth (i.e., twice the Rayleigh Range) of our laser spot (480 μ m) is much higher than the typical roughness (Ra = ~10.6 μ m) value of the as-printed additive samples.

¹ Department of Electrical and Computer Engineering, Auburn University, Auburn, Alabama 36849, United States.

² The Department of Biomedical Materials Science, University of Mississippi Medical Center, Jackson, Mississippi 39216, United States.

³ Department of Mechanical Engineering, Auburn University, Auburn, Alabama, 36849, United States.

⁴ National Center for Additive Manufacturing Excellence (NCAME), Auburn University, Auburn, Alabama 36849, United States.

^{*}Address correspondence to mahjouri@auburn.edu

Figures SI, S2, and S3 show the Raman spectra, optical and SEM images of additively manufactured TAV samples, respectively. The results confirm the successful formation of anatase, rutile, and mixed rutile/anatase phases. Anatase samples showed clear Raman peaks at 145, 198, 399, 516, and 638 cm⁻¹, while rutile samples showed peaks 241, 445, 610 cm⁻¹. The samples with mixed-phases have the signature of both anatase and rutile.

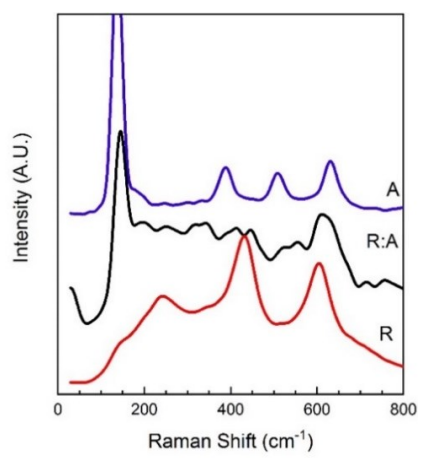


Figure S1. Raman spectra of the synthesized TiO₂ structures on additively manufactured samples showing the successful formation of anatase, mixed-phase, and rutile peaks.

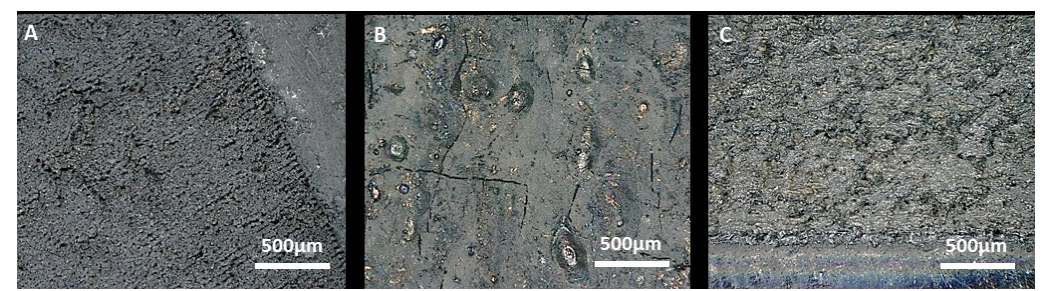


Figure S2. Optical images of anatase, (a), mixed-phase (b), and rutile (c) structures formed on the additively manufactured samples.

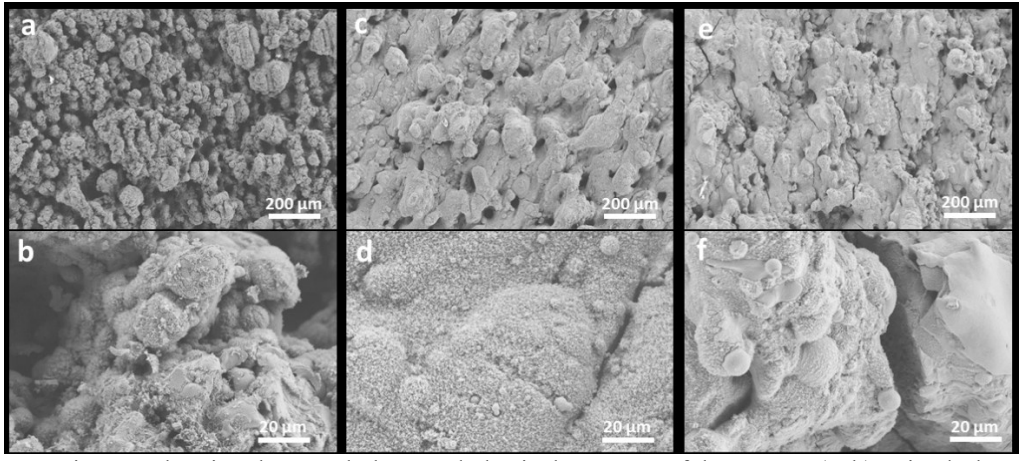


Figure S3. SEM images showing the morphology and physical structure of the anatase (a, b), mixed-phase (c, d), and rutile (e, f) samples structures formed on the additively manufactured samples. Smaller features with micro/nanostructures and mesoporous morphology were observed for anatase samples. The feature became larger and denser for rutile samples.

High Purity Wrought Ti Samples:

Figures S4, S5, and S6 show the Raman spectra, optical, and SEM images of laser-treated high purity titanium samples, respectively. The results confirm the successful formation of anatase, rutile and mixed rutile/anatase phases.

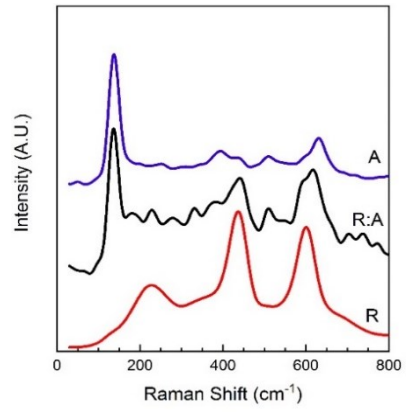


Figure S4. Raman spectra of the synthesized TiO₂ structures on pure titanium samples showing the successful formation of anatase, mixed-phase, and rutile peaks.

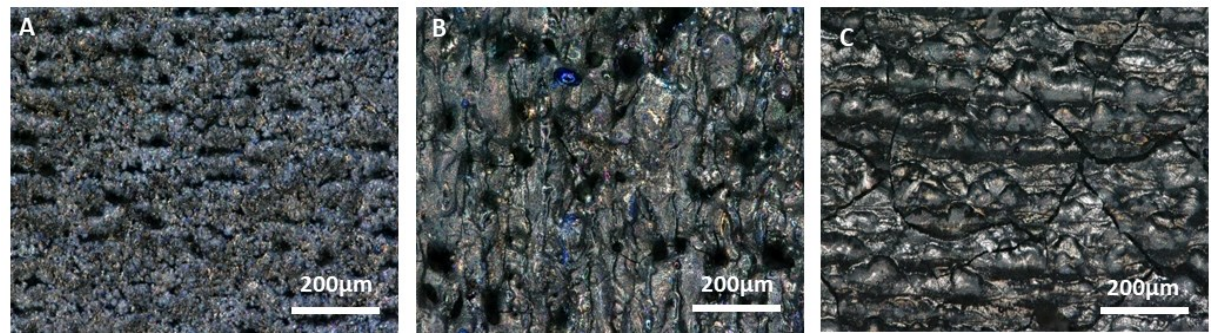


Figure S5. Optical images of anatase (a), mixed-phase (b), and rutile (c) formed on the pure titanium samples.

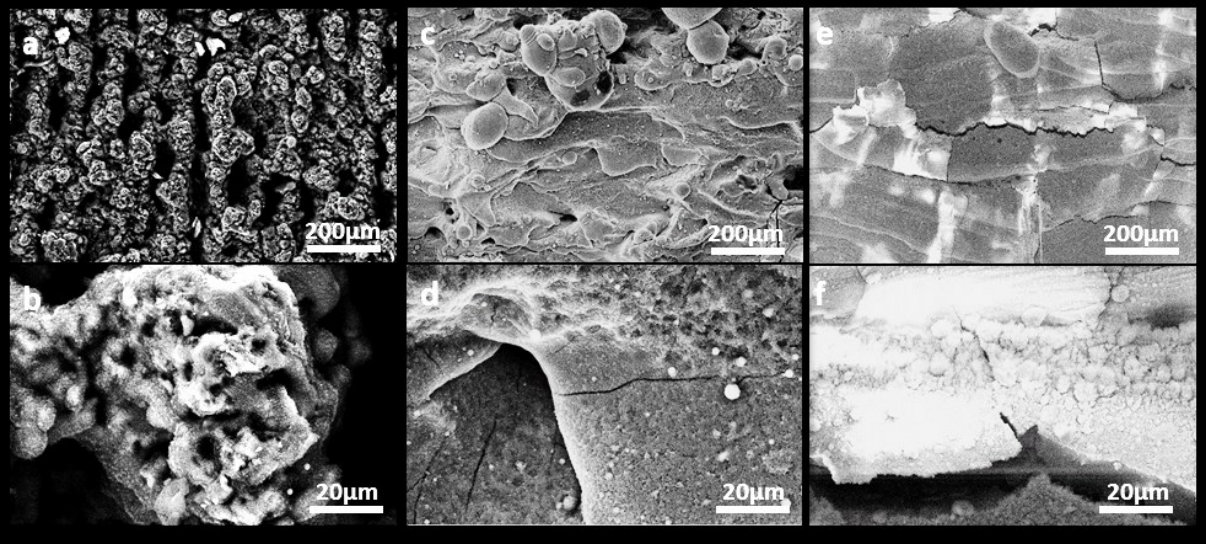


Figure S6. SEM images showing the morphology and physical structures of the TiO₂ anatase (a, b), mixed-phase (c, d), and rutile (e, f) nanostructures. Smaller features with micro/nanostructures and mesoporous morphology were observed for anatase samples. The feature became larger and denser for rutile samples.

Wrought CP Ti Grade 4 Samples:

Figure S7 shows the Raman spectra of the anatase, rutile, and mixed-phase on CP Ti.

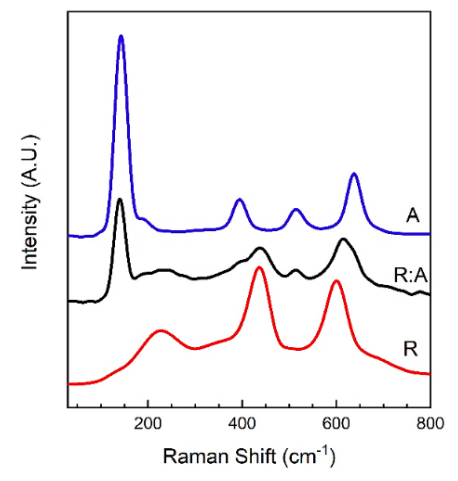


Figure S7. Raman spectra of the synthesized TiO₂ structures on CP Ti samples showing the successful formation of anatase, mixed-phase, and rutile peaks.

Cross-Section SEM Images of wrought TAV

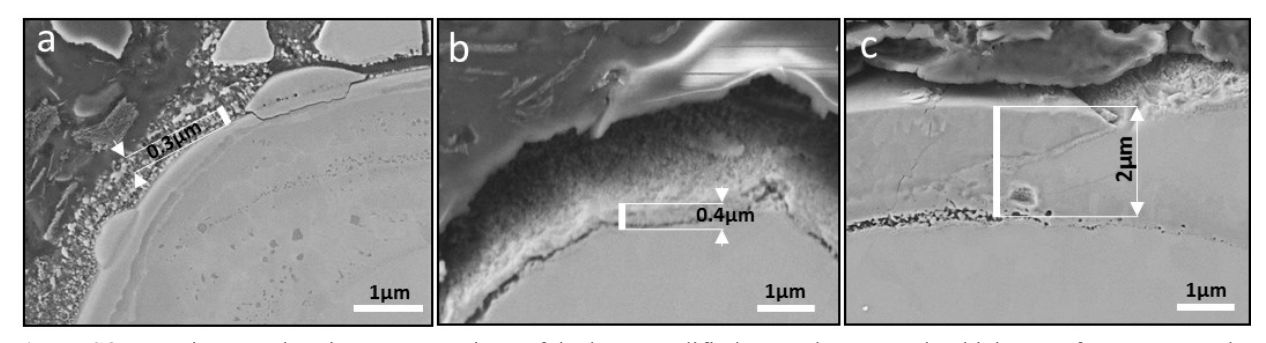


Figure S8. SEM images showing cross-sections of the laser modified wrought TAV. The thickness of anatase samples (\sim 0.3 µm) was the smallest, whereas the thickness became larger for mixed (\sim 0.4 µm) and rutile (\sim 2 µm), respectively.

TiO2 Quality Comparison - laser-generated TiO2 versus commercial powers

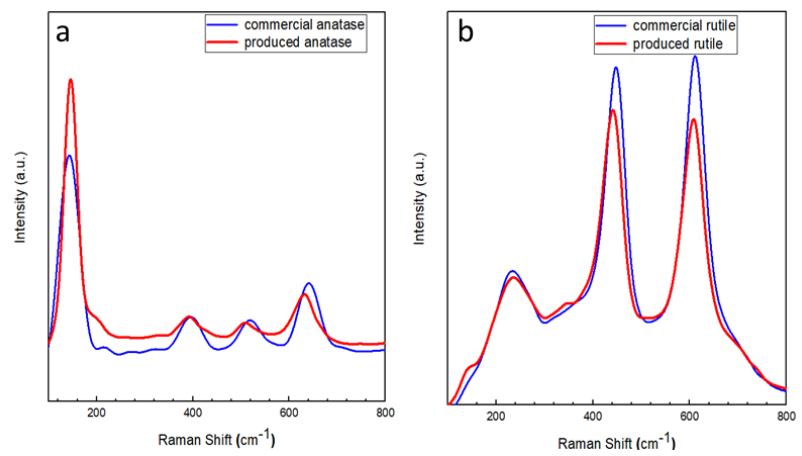


Figure S9. TiO₂ quality comparison of the laser-generated versus the commercially available anatase (a) and rutile (b) samples, both showing similar Raman signatures.

Roughness Values before Laser Processing

The pure and wrought samples had smoother surfaces than the as-printed additive samples. Representative surface roughness (Ra) values for pure titanium, wrought TAV, and additive samples were $0.25~\mu m$, $0.27~\mu m$, and $10.6~\mu m$, respectively.

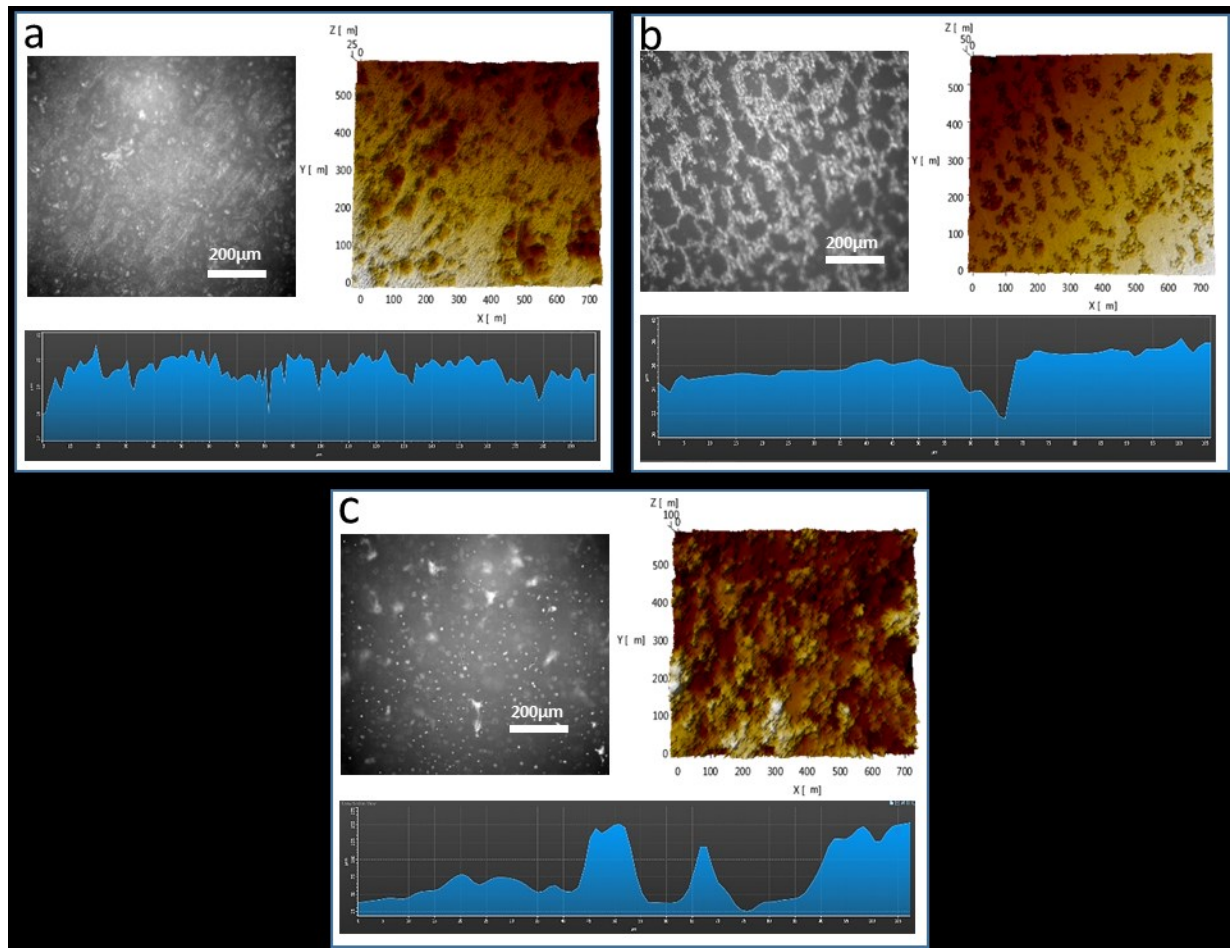


Figure S10. Representative laser confocal 2D images and 3D surface profiles of pure titanium (a), wrought TAV (b), and additively manufactured (c) samples. The surface roughness (Ra) values for pure titanium, wrought TAV, and additive samples were $0.25 \mu m$, $0.27 \mu m$, and $10.6 \mu m$, respectively.